Progressive failure monitoring and analysis in aluminium by in situ nondestructive evaluation

Brian J. Wisner, Philipp Potstada, Vignesh I. Perumal, Konstantinos P. Baxevanakis, Markus G. R. Sause, Antonios Kontsos

Angaben zur Veröffentlichung / Publication details:

Wisner, Brian J., Philipp Potstada, Vignesh I. Perumal, Konstantinos P. Baxevanakis, Markus G. R. Sause, and Antonios Kontsos. 2019. "Progressive failure monitoring and analysis in aluminium by in situ nondestructive evaluation." *FFEMS - Fatigue & Fracture of Engineering Materials & Structures* 42 (9): 2133–45. https://doi.org/10.1111/ffe.13088.

Progressive failure monitoring and analysis in aluminium by in situ nondestructive evaluation

Brian J. Wisner[1] Philipp Potstada[2] Vignesh I. Perumal[3]
Konstantinos P. Baxevanakis[4] Markus G. R. Sause[2] Antonios Kontsos[3]

[1] Department of Mechanical Engineering, Russ College of Engineering and Technology, Ohio University, Athens, Ohio

[2] Mechanical Engineering, Institute for Materials Resource Management, University of Augsburg, Augsburg, Germany

[3] Theoretical and Applied Mechanics Group, Department of Mechanical Engineering and Mechanics, College of Engineering, Drexel University, Philadelphia, Pennsylvania

[4] Wolfson School of Mechanical, Electrical and Manufacturing Engineering, Loughborough University, Loughborough, UK

Correspondence
Antonios Kontsos, Theoretical and Applied Mechanics Group, Department of Mechanical Engineering & Mechanics, College of Engineering, Drexel University, Philadelphia, PA.
Email: antonios.kontsos@drexel.edu

Funding information
Young Investigator Program, Grant/Award Number: N00014-14-1-0571

Abstract

Damage initiation and progression in precipitate hardened alloys are typically linked to the failure of second phase particles that result from the precipitation process. These particles have been shown to be stress concentrators and crack starters as a result of both particle debonding and fracture. In this investigation, a precipitate hardened aluminium alloy (Al 2024-T3) is loaded monotonically to investigate the role the particles have in the progressive failure process. The damage process was monitored continuously by combining the acoustic emission method either with in situ scanning electron microscopy or X-ray microcomputed tomography to obtain both surface and volume microstructural information. Particles were observed to fracture only in the elastic regime of the material response, while void growth at locations predominantly near particles were found to be associated with progressive failure in the plastic region of the macroscopic response. Experimental findings were validated by fracture simulations at the scale of particle-matrix interface.

KEYWORDS

acoustic emission, aluminium, fracture, nondestructive evaluation, plasticity, X-rays

1 INTRODUCTION

Material damage is a stochastic process that bridges multiple scales including initiation, nucleation, and growth. Often, damage investigations are conducted at the lab scale and focus on the growth of damage in the form of cracks.[1-6] More recently, a number of investigations have attempted to link changes at the macroscopic mechanical behaviour with post mortem microstructural observations.[7-10] In several cases nondestructive evaluation tools have been used to enhance the understanding of material evolution beyond such load curves and post mortem investigations. Particularly, digital image correlation (DIC) has been proven useful to identify strain concentrations that appear on the surface during loading allowing for more detailed investigations of microstructural changes; however, these investigations largely remain ex situ.[6,9,11-13] In addition to the observation of surface changes, the acoustic emission (AE) technique has also been used in situ, during loading, to identify changes in the material both on and below the surface.[5,12,14-23]

In this context, various features extracted from AE data such as amplitude, duration, and frequency content have been related to individual damage sources by

identifying the material changes at a range of scales, in particular for particle fracture in aluminium,[17,19,21-24] twinning in magnesium,[8,9,11,20] and fibre breakage in composites,[15,25,26] among others.[27,28] Specifically, the coupling of DIC and AE has been shown by the authors of this investigation to be effective in identifying damage and its location in lab-scale experiments, which lead to validated conclusions especially in the case of crack initiation in aluminium alloys.[13,14]

Moreover, the development of small-scale loading devices capable of fitting inside a scanning electron microscope (SEM), for example, allows for the observation of microscale surface changes directly at the time and scale they occur. In this type of investigations, the coupling of in situ SEM observations with AE and DIC as previously reported by the authors made possible the direct linkage of recorded AE waveforms with the activation of damage sources at relevant time and length scales, ie, at the microstructural level.[20,22-24,29-31] Using this approach, particle fracture in aluminium alloys was identified by the authors to be a predominant early damage mechanism the activation of which was confirmed by combining AE, DIC, and SEM data in time intervals in which all three such datasets were available.[22-24]

Beyond surface observations, in situ X-ray microcomputed tomography (μ-CT) has been used to observe the evolution of damage in all three spatial dimensions over time. Specifically, this technique has been used to examine crack growth in aluminium,[32-35] fibre breakage in fibre-reinforced composite materials,[26,36] and to observe void formation and growth in aluminium due to thermal loads.[37] In addition to observing the three-dimensional damage evolution, efforts have been made to couple in situ μ-CT investigations with in situ AE monitoring.[26,38-40] This linkage between a qualitative but relatively fast in terms of acquisition rate volume inspecting damage detection tool (AE) and a full-field three dimensional imaging tool (μ-CT), which, however, has slower acquisition rates, provides the possibility to validate AE activity recorded in aluminium alloys and was previously attributed to particle fracture.

Consequently, this paper leverages the prior related work by the authors to investigate the nucleation and evolution of damage in aluminium 2024-T3 by combining in situ X-ray μ-CT measurements with simultaneously recorded AE data and by comparing such findings with corresponding measurements obtained by combining AE with in situ SEM testing and monitoring. Specific hypotheses related to the particle spatial distributions and the associated formation of voids near them are tested and are found to provide unprecedented insights to the progressive development of this ductile failure process. A related computational model is finally employed to explain the prevalence of particle fracture over particle-matrix debonding.

2 | EXPERIMENTAL PROCEDURE

2.1 | Material

An aircraft grade precipitate-hardened aluminium 2024-T3 rolled sheet with a 2.5 mm nominal thickness was used in this investigation. The aluminium was used in the as-received condition, which contains up to 5% Cu, 1.8% Mg, 1% Mn, 0.5% Fe, 0.5% Si, and trace amounts of Cr and Zn. The particles present in the aluminium were examined by energy-dispersive spectroscopy; the chemical content was identified as primary particle types including Al_7Cu_2Fe, Al_2CuMg, and Al_2Cu, which agrees with related information in the literature.[41-43]

2.2 | Specimen preparation

Two specimen geometries were used for this work and are shown in Figure 1. The gage section of both specimens contains an hourglass-shaped section designed with a radius of curvature of 4 mm to localize damage for in

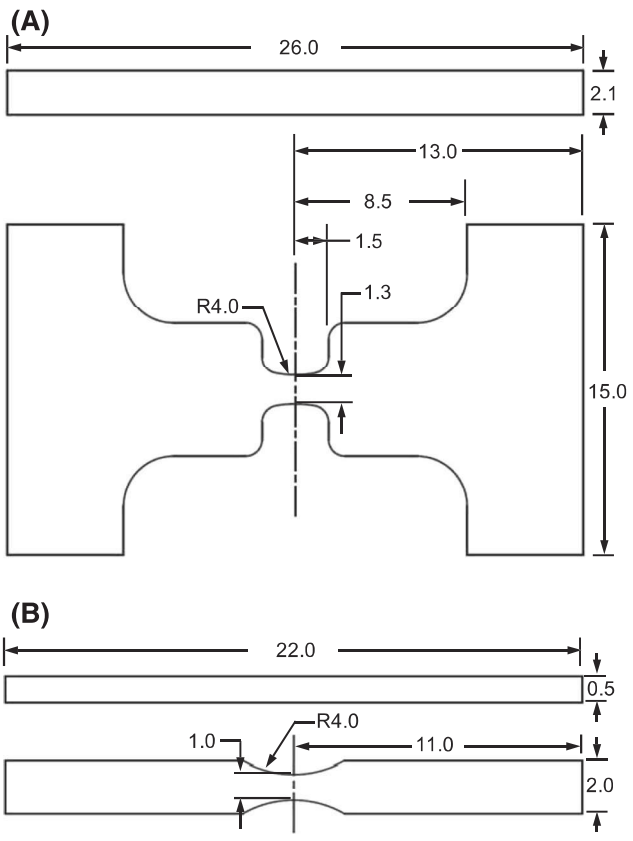

FIGURE 1 Specimen geometry for (A) ex situ and (B) in situ X-ray quasi-static monotonic loading with acoustic emission

situ observations without inducing significant geometric effects. The gage section is nominally 3 mm long and 2.5 mm thick with the narrowest section at 1.3 mm for the larger specimen shown in Figure 1A. This specimen was used for in situ SEM observations coupled with ex situ X-ray μ-CT investigations.[22] As such, the surface is mechanically ground and polished to 0.05 μm alumina suspension resulting in a final thickness of 2.0 mm. In addition, specimens using the same hourglass-shaped section were designed for the in situ X-ray μ-CT investigations (Figure 1B) with the smallest cross section of the specimen at 0.5 mm × 1 mm to ensure that specimen failure occurred given the load frame used in this setup. These specimens were ground to approximately 1 μm surface roughness before testing.

2.3 | Mechanical and nondestructive test setup

Mechanical testing inside the SEM was accomplished using a GATAN MTEST equipped with a 2.1 kN load cell at a displacement rate of 0.1 mm/min. A 50 μm^2 field of view was monitored using secondary electron imaging; a total of sixteen 50 μm^2 windows were imaged during load holds. AE was recorded during the entire loading sequence using two PICO sensors (with operating frequency in 150–750 kHz range). The AE data were recorded using a PCI-2 data acquisition board with a threshold of 25 dB using a 100 to 2000 kHz band-pass filter and 50/300/300 PDT/HDT/HLT settings at a sampling rate of 10MSPS (million samples per second). All signals were passed through a 2/4/6 preamplifier set to provide a uniform 40 dB preamplification across all frequencies. All hardware and software used for AE monitoring is provided commercially by MISTRAS Inc.

Ex situ X-ray scans were performed on this specimen at the pristine condition as well as after loading at 375 MPa, unloading and removing the specimen from the load stage. These ex situ scans were performed using a SkyScan 1272 system with a source voltage of 80 kV, a current of 125 μA, and an exposure time of 5.5 seconds. Images were taken every 0.1° through a full 360-degree rotation resulting in a voxel size of 1.65 μm.

In situ X-ray data were recorded while applying tensile loading using a customized CT500 electromechanical loading stage equipped with a 500-N load cell at a rate of 0.2 mm/min (manufactured by Deben Co. Ltd.). Displacement was measured by the cross head motion resulting in some compliance issues at the early stages of loading. The stage was located inside a Nanotom 180 m (manufactured by GE). Figure 2A shows a sample load curve used for the investigation.

Before each scan, the load was slightly reduced (as shown in Figure 2A) to allow for material relaxation. During the scans the applied displacement was held constant to sustain the deformation induced on the specimen. Since the load was not removed, full three-dimensional observations of the particle distribution and void and evolution were possible to be made. The X-ray scan was performed at 100 kV resulting in a voxel size of 2.3 μm. Selected load steps were scanned at higher voxel resolution of 1.1 μm to inspect the microstructure in detail. The full details of the X-ray source settings, scan parameters, and analysis software are given in Table 1.

An example for the obtained particles distribution is shown in Figure 2B. The X-ray reconstructed slices were further used in a digital volume correlation (DVC) analysis performed using a commercially available DVC software (VIC-Volume produced by Correlated Solutions, Inc). For the analysis, a subset of 85 voxels and step size of 40 voxels was used. Segmentation of each image was

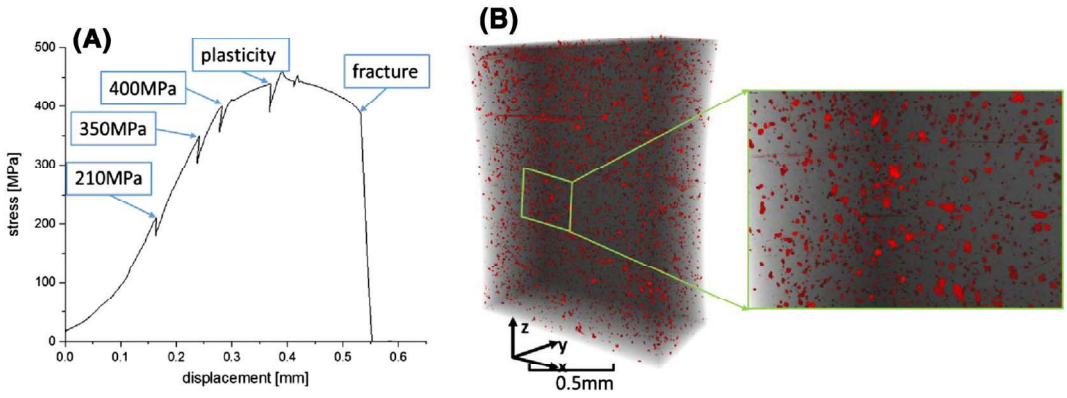

FIGURE 2 A, Load curve with load hold values marked. B, Initial particle distribution [Colour figure can be viewed at wileyonlinelibrary.com]

TABLE 1 X-ray characteristics for in situ scans coupled with mechanical testing

CT:	Standard Resolution	High Resolution
Voltage, kV	100	
Current, μA	120	
Exposure time, s	2	10
#images	10 001 000	
Voxel size, μm	2.3	1.1
Reconstruction software	GE phoenix datos|x	
Analyzing software	VGSTUDIO MAX 2.1	

performed using a custom algorithm based on a gradient and gray scale threshold to identify particles, voids, and base aluminium. A gradient map for each slice was obtained using the Sobel operator to identify edges based on sharp gradients and eliminating the gradients resulting from white noise. The area bounded by the edges was identified as either particle or void based on a gray value threshold. For this work, particles were represented by saturated pixels at or near a gray value of 255, while voids were represented by pixels at or near a gray value of 0. As the gradient method identified the edges of either a void or particle, a gray value of 100 was selected as the threshold for the binary classification of void or particle.

AE was monitored during the entire loading sequence via a KRNBB-PC (KRN services) sensor attached to the sample via a wave guide as introduced in [40]. Signals were amplified by a 2/4/6 preamplifier with bandwidth from 20 to 1,200 kHz and were recorded by a PCI-2 card at 35 dB threshold at 60 dB preamplification and 10/200/300 PDT/HDT/HLT settings.

3 | RESULTS

3.1 | Progressive failure monitoring by in situ SEM level testing combined with AE

Monotonic loading was applied to the specimen for the SEM part of the investigation. Figure 3 shows the typical AE activity for the specimens in Figure 1A. The highest amplitude AE hits occur below 325 MPa, which is below the yielding point. Figure 3B presents a typical waveform observed during the early stages of loading, while Figure 3C shows a typical waveform observed closer to the end of the loading.

For this experiment, the load was stopped just after the yield strength, at 375 MPa, ie, after the high-amplitude AE signals were observed and detailed surface investigations along with an ex situ X-ray micro–computed tomography was performed. This procedure targeted the identification of damage mechanisms that were responsible for the observed AE activity. In this context, Figure 4

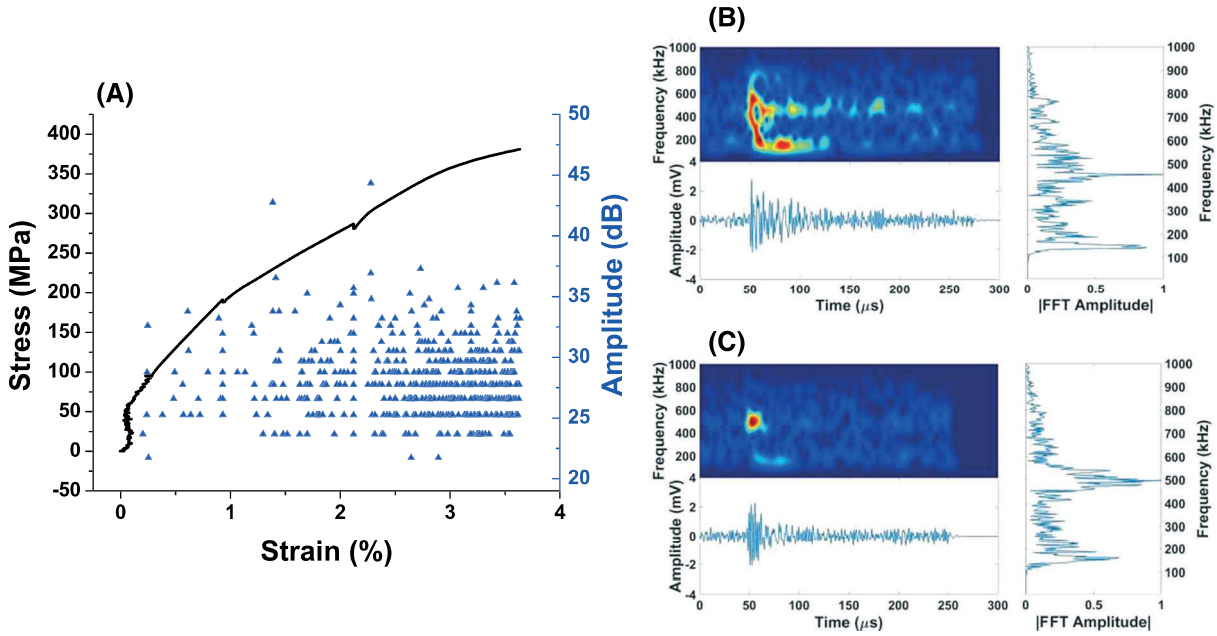

FIGURE 3 A, Stress strain curve for a typical scanning electron microscopy (SEM) test overlaid with the acoustic emission (AE) activity. B and C, Examples of AE waveforms observed during mechanical loading inside the SEM [Colour figure can be viewed at wileyonlinelibrary.com]

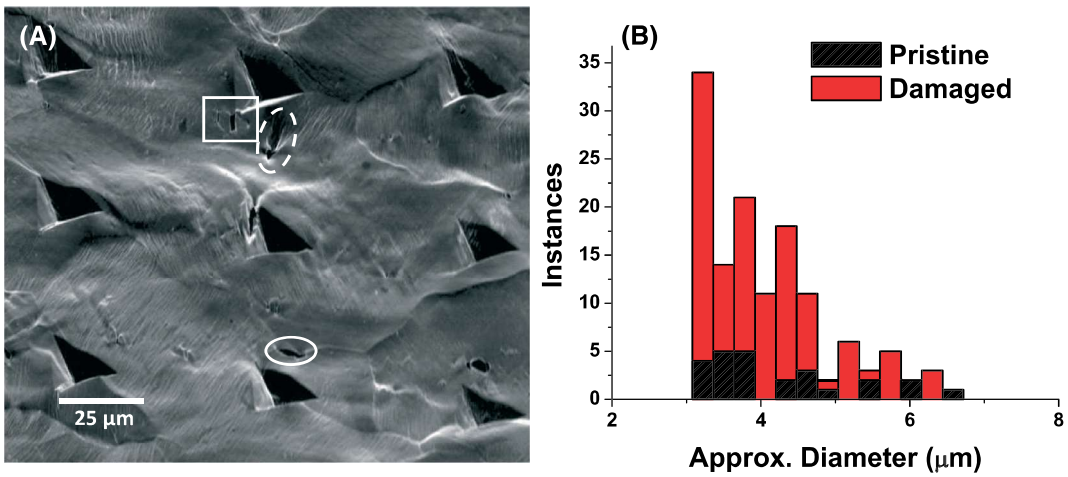

FIGURE 4 A, Scanning electron microscopy (SEM) micrograph of the monitored surface during in situ SEM loading taken after removing the load. B, Void evolution obtained from X-ray micro–computed tomography [Colour figure can be viewed at wileyonlinelibrary.com]

revealed a number of expected damage mechanisms for this metal within the monitored region. Specifically, the surface was found to be rough, which is a characteristic of ductile failure. In addition, several slip lines (observed as lighter gray lines visible everywhere in the region), as well as voids (indicated by the white boxes) produced by particle fractures, slip bands (indicated by the dashed white ellipse), and by grain boundary interactions (indicated by the solid ellipse) were observed. Comparison of the X-ray scan before and after loading was used to quantify the change in void density as a result of damage. The histogram in Figure 4B reveals a significant increase in the number of voids as a result of loading, which agrees with previous work by the authors.[22]

Given the results in this section, it was concluded that void density evolution can be tracked by the combination of methods used; however, relating the evolution of such void density in the volume with the in situ recorded AE activity and the stress–strain curve of Figure 3 is not feasible unless in situ X-ray data are obtained, which is the focus of the following section.

3.2 | Progressive failure monitoring by in situ X-ray µ-CT level testing combined with AE

Tensile loading was applied for the in situ X-ray investigations with load holds at several time instances (as marked in Figure 2 and marked in Figure 5) to allow for X-ray scans. A sample load curve overlaid with AE activity that is representative of the results obtained in this part of the investigation is shown in Figure 5. These results were found to be consistent with the corresponding ones reported in Figure 3. In the case of the in situ X-ray investigation presented in this section, the AE

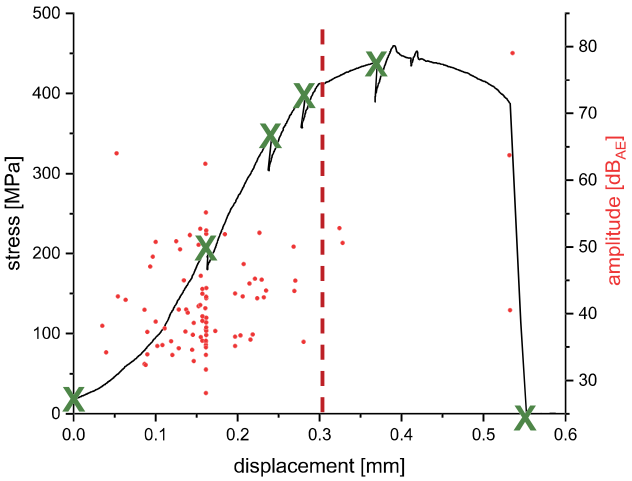

FIGURE 5 Stress-strain curve overlaid with acoustic emission activity for the in situ X-ray investigation [Colour figure can be viewed at wileyonlinelibrary.com]

activity with the highest amplitude signals occurred below 350 MPa and hence prior again to yielding which is indicated by the dashed line. In addition, Figure 5 shows fewer recorded AE signals compared with Figure 3, which can be explained by the sensitivity of the selected sensor, the waveguide required to record in situ AE signals with this setup, and the smaller specimen size. The data trends, however, remain similar including increased activity in the elastic regime, which becomes even more pronounced near yielding. After yielding, the fewer AE signals indicate a potential change in the damage mechanism; this agrees with the trends observed in the SEM tests.

The objective of this investigation is to link the obtained mechanical behaviour and nondestructive evaluation measurements with the evolution of surface microstructure (via in situ SEM observations) as well as

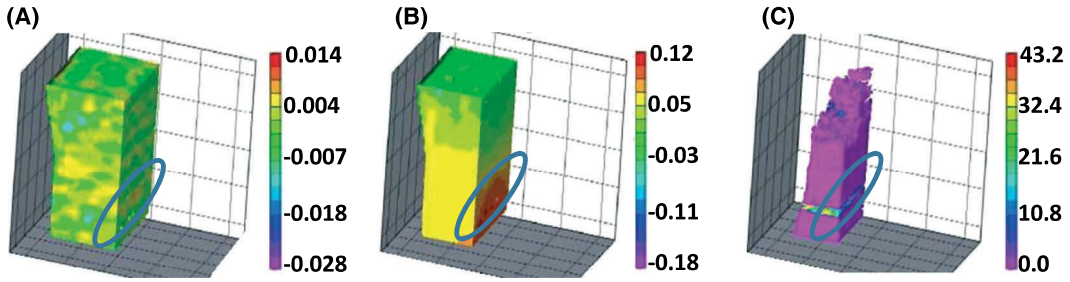

FIGURE 6 Full field strain evolution inside the volume of the specimen at A, the elastic region B, near yielding, and C, at fracture [Colour figure can be viewed at wileyonlinelibrary.com]

the evolution of subsurface damage (via the X-ray micro–computed tomography). In this context, Figure 6 shows the evolution of longitudinal strain within the volume of the material using DVC. The results show that no significant strain accumulation is observed until after the yield point with the largest strain accumulation occurring below the surface. This subsurface dominated evolution of strain is expected from a ductile fracture process perspective and can be linked to specific damage mechanisms by examining the observed damage within each X-ray scan slice. After fracture, the strain inside the volume of the material relaxes with the exception of the area right around the fracture zone that appears permanently deformed.

Figure 7 shows an example of one subsurface X-ray slice taken about halfway through the thickness and at a near yield stress. Microstructural features such as particles are observed as bright spots, while voids appear as black spots and the aluminium matrix is depicted in gray. Two fractured particles were observed, which are circled in red. One appears well inside the specimen, while the other is observed at the edge and a crack appears to have initiated from it. Additionally, voids appear to be forming predominantly in the middle of the specimen, as expected in a progressive ductile failure process, while a few other scattered voids can be observed throughout the width. Upon closer examination, some of the observed voids were found on the boundary between a particle and the matrix as indicated at the locations marked within green boxes. Additional voids were found within the matrix, near grain boundaries, or other defects.

The microstructural evolution as a function of the progressive failure process can be tracked by comparing the X-ray reconstructed specimens to the pristine scan obtained prior to loading. Figure 8 shows such results obtained at 400 MPa (Figure 8A), after yielding (Figure 8B), and after fracture (Figure 8C). Minimal damage is observed prior to the yield point despite the AE activity trend suggesting that damage is possible to have initiated somewhere else within the microstructure. The lack of X-ray observation of damage at this load is expected as the SEM results reported earlier in this manuscript reveal fractures on the same length scale or smaller compared with the scan resolution making the detection of such fractures via X-ray tomography challenging at this scale. However, one particle fracture indicated in the green circle is observed during the initial plasticity stages along with the appearance of small voids. Most void formation and growth, however, is observed to occur between Figures 8B and 8C, which corresponds to

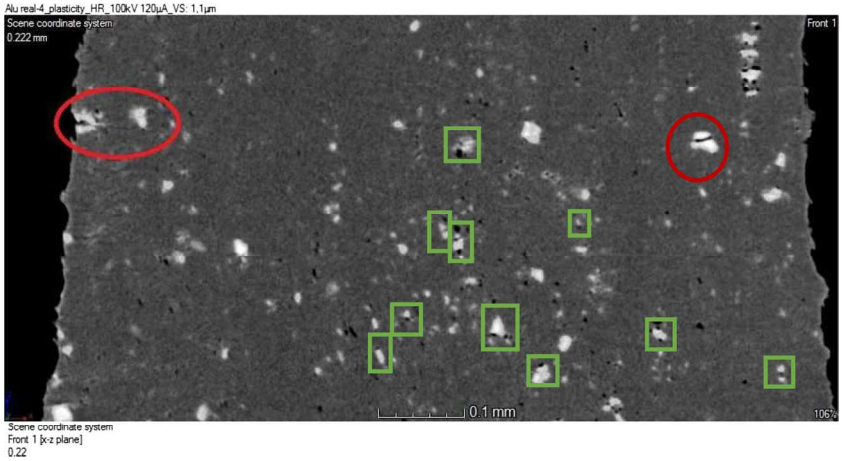

FIGURE 7 X-ray scan showing a crack nucleating through a fractured particle on the edge and a subsurface fractured particle [Colour figure can be viewed at wileyonlinelibrary.com]

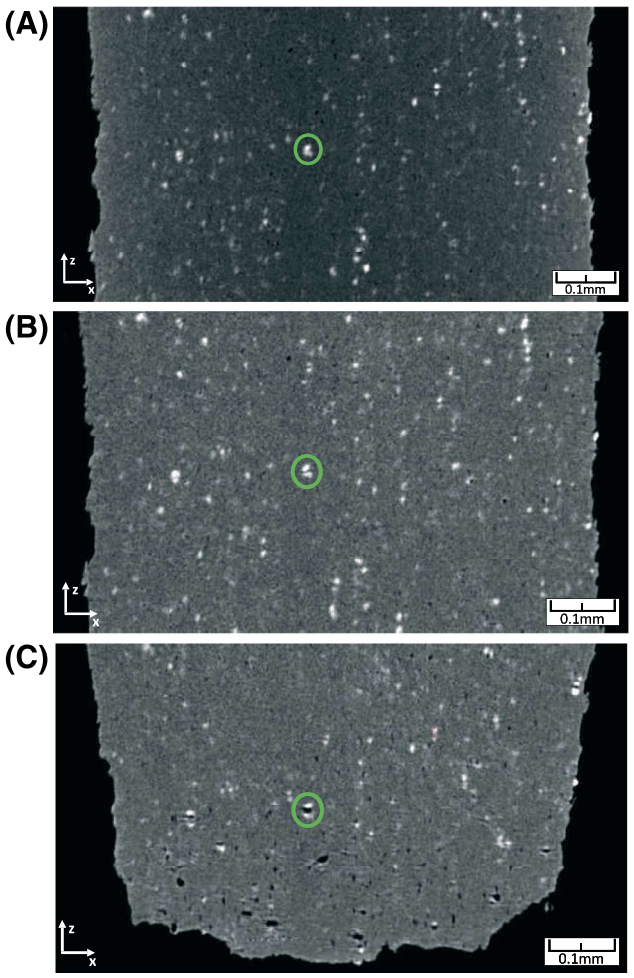

FIGURE 8 Evolution of fractured particles at A, at 400 MPa, B, after yielding MPa, and C, after fracture [Colour figure can be viewed at wileyonlinelibrary.com]

the plastic region of the stress strain curve and suggests that fractures have grown larger than the minimum scan resolution allowing for detection. Therefore, a shift occurs after the yield point from initial fracture to growth events explaining the reduction in the number of high amplitude AE events observed in both SEM and X-ray results. Most of the void formation is observed to occur near the final fracture, and the largest voids are observed below the surface as expected from a ductile failure response and as observed in the DVC results.

The evolution of the voids size and shape in full three-dimensional space was evaluated using the segmentation algorithm discussed in Section 2.2 to allow for a quantitative evaluation of the void evolution; the related results are shown in Figure 9. Specifically, the average size of the voids is found to increase as a function of loading as shown in Figure 9A.

The total void density, as discussed earlier, is the result of both particle fractures as well as debonding of the particles from the matrix. However, as mentioned earlier, voids smaller than a few microns are challenging to be observed due the imaging resolution. The void distribution was further examined by calculating the distance between voids and particles with the objective to identify the fraction of those voids nucleated near particles, which is a characteristic of the progressive ductile damage process. Figure 9B shows the computed distance values between all identified voids and the nearest particles. These values were obtained by measuring the distance between the centroids and subtracting the approximate radius of the void and particle. The approximate radius of both voids and particles was determined by defining a sphere that contains the same volume as the measured voids and particles. Small distance values suggest that the formation of voids was the result of particle-matrix interaction or particle-matrix decohesion such as the ones shown in Figure 7. Moreover, larger distances suggest that voids form as the result of another mechanism such as dislocation buildup on high misorientation angles between grain boundaries. As shown in Figure 9B, the majority of such distances

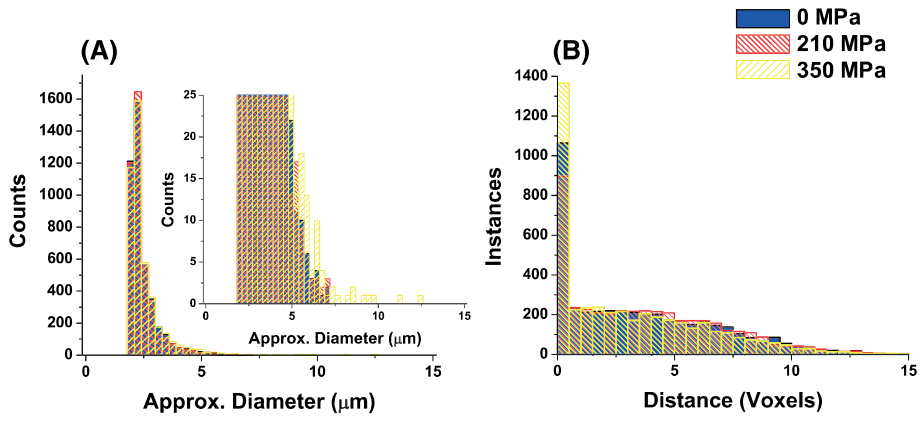

FIGURE 9 Evolution of A, void size and B, distance between particles and void as a function of load step [Colour figure can be viewed at wileyonlinelibrary.com]

is smaller than 1 voxel, while more of those distances were found to be in that range with increasing load, which suggests that voids were nucleated near particles, which corroborates with what was expected for a ductile damage process and further justifies the AE activity of Figure 5.

In addition to identifying the link between particles and the location of void nucleation, the evolution of the void shape was quantified and pertinent results are shown in Figure 10 by fitting an ellipsoid to the voids and plotting each of the principle axes against the approximate diameter if a sphere was fit to the same volume. A void would grow spherically if the length measured in each axis was equal to the approximate sphere diameter. However, it can be seen in Figure 10 that as further loading is applied, the size of the voids increases and a larger deviation between the principle axes and the approximate diameter is observed. More specifically, the first two principle axes are observed to be much larger than the approximate diameter, while the length of the third axis is smaller indicating voids becoming wider and thinner especially after yielding (>350 MPa).

4 | DISCUSSION

The stored energy during the ductile damage process is redistributed as a result of local microstructure changes associated with plasticity and damage. In the case of precipitate-hardened materials such as the Al 2024-T3 investigated, the harder and stiffer particles that are added to increase the strength of the material carry most of the applied load while the Al matrix surrounding the particles has higher strain.[22,24,43] This effect caused by the mismatch in material properties has been demonstrated to lead to particle fracture.[23,24,31] In addition, previous work by the authors using in situ SEM observations coupled with AE activity and DIC strain measurements under both monotonic and cyclic loading provided quantitative evidence related to such connection.[23,24,31] In particular, particle fracture was observed to produce detectible AE activity that was linked directly to the observation of such fracture events.

The AE activity presented in this manuscript and the in situ microstructural observations provided by X-rays indicate that the initial stages of damage occur prior to yielding and are the result of particle fracture. These particles are strong (compared with the surrounding matrix) but brittle, and consequently, as the material deforms, these particles carry the majority of the applied load. Hence, the results in this investigation suggest that prior to yielding, particle fracture is the dominant mechanism leading to the formation of voids. Additional voids were also seen to appear as the result of dislocation buildups and debonding between particles and the aluminium matrix; however, such voids do not seem to occur until or after the yield point.[2] After yielding, it was shown (e.g., Figure 8) that void growth controls the damage progression. Void growth at this scale is expected to be a less dominant AE source due to both the size of the voids as well as because void growth is a less abrupt effect compared with particle fracture; this remark partially explains why the AE activity is drastically reduced in the plastic region (see, eg, Figure 5). Previous studies have shown large amounts of AE activity in this region, but these studies were conducted on larger specimens where the crack is large enough to produce detectible AE signals.[1,13]

To further elaborate on this point, ie, the competing ductile fracture mechanisms and their associated energy, the authors previously utilized physics-based finite element modelling to examine the effect of material properties and associated particle or matrix fracture to provide a theoretical justification for the in situ observed microstructural changes reported in their work.[24] To expand on such theoretical investigation, a crystal plasticity finite element method (FEM) approach coupled with an XFEM formulation was used to conduct a wave propagation investigation and simulate the physical sources of AE in the ductile fracture process investigated in this manuscript. Details on the way these simulations were set up

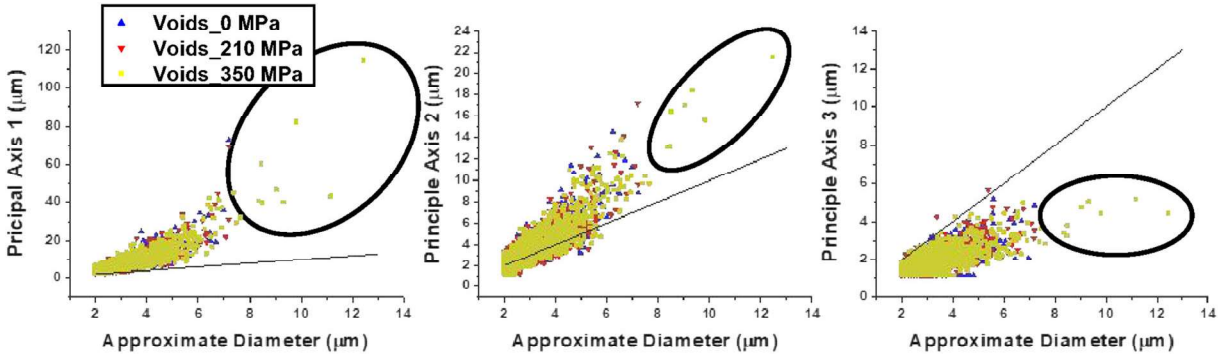

FIGURE 10 Void shape evolution as a function of loading [Colour figure can be viewed at wileyonlinelibrary.com]

are provided in Appendix A for completeness; however, emphasis is given herein on the results of such numerical analysis. For this study the particle was assumed to be a 10 μm diameter sphere embedded in a 1000 μm single crystal of aluminium (Figure 11A). By treating the particle as a homogeneous material and changing the modulus of the aluminium matrix to simulate hard and soft crystal orientations, the fracture location was observed to change, while the size of the fracture remained approximately consistent as seen in Figure 11B.

A softer matrix would result in a shift of the damage mechanism from particle fracture to matrix fracture or particle debonding as also shown in Figure 11B. In both cases the size of the fracture zone was found to be about the same (2.16 μm for particle and 2.73 μm for matrix fracture).

To better quantify parameters associated with the stress wave induced by such fracture events, the full field wave propagation for the case of particle fracture is shown in Figure 11A. The XFEM implementation in the commercial software Abaqus requires an implicit FE formulation. As a dynamic analysis is computationally expensive, a coupled simulation technique in Abaqus is used-one which uses an implicit formulation for the particle domain and an explicit formulation for the matrix domain. Further, it couples the parts using a lock-step coupling scheme as explained by the Abaqus User Manual.[44] In a lock-step co-simulation, each individual simulation undergoes an increment independently and then the communication between the simulations take place after each increment, as in the lock-step method or after a number of increments as determined by the analysis in the subcycling method. A quasi-static displacement boundary condition of 1.729 μm was determined to be sufficient to attain the required stress state to initiate fracture in the domain. The final model of 962 500 nodes would have been computationally expensive to run as the fracture initiation using XFEM requires an implicit domain. To this aim, a quasi-static step with mass-scaling was considered in the explicit domain to simulate the load increment till fracture. The time increments were set to 0.1 ns to completely resolve the wave signals for a duration of 100 ns.

Although all three components of displacement, velocity, and acceleration could be computed, in this case the velocity component in the *x*-direction (V1) is plotted in Figure 11C as a function of time demonstrating the wave propagation in the form of travelling wavefronts. Figure 12 provides additional information related to wave propagation shown in Figure 11C by plotting the time

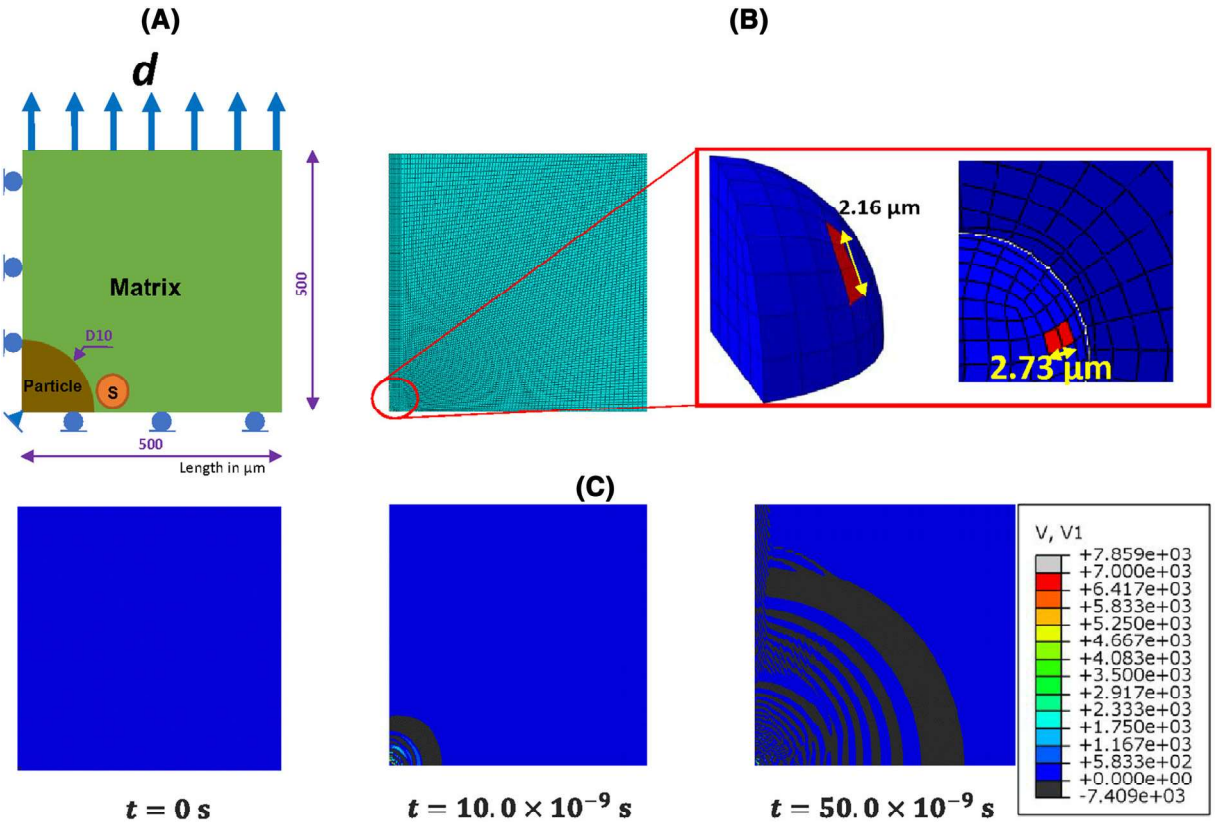

FIGURE 11 A, Finite element analysis boundary value problem used to investigated the competing ductile fracture mechanisms; B, the two possible damage mechanisms including particle and matrix fracture; C, stress wave propagation following a particle fracture event [Colour figure can be viewed at wileyonlinelibrary.com]

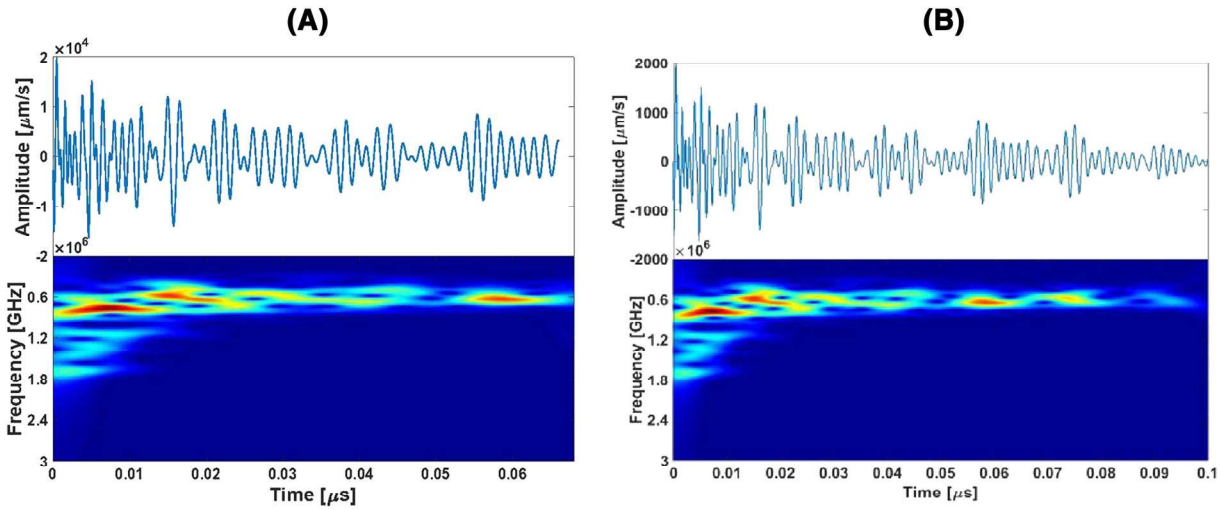

FIGURE 12 Amplitude and frequency evolution (wavelet transform) of the wave propagation induced by A, particle fracture and B, matrix fracture [Colour figure can be viewed at wileyonlinelibrary.com]

series representing the oscillation of a single point near the particle-matrix interface marked with "S" in Figure 11.

In the waveforms of Figure 12 the most interesting remark that can be made is the fact particle fracture events appear to produce waves with an amplitude that is found to be an order of magnitude higher compared with the matrix fracture case, which provides theoretically evidence related to the AE from void formation near the particle-matrix interface and the challenges to detect it, as mentioned earlier. It should also be noted that the frequency range (GHz) of the waveforms shown in Figure 12 can be explained by the length scale of the fracture source (~2 μm) of ductile fracture that leverage AE,[5,6] while the fact the experimental AE data are in a different range (kHz) can be explained by attenuation (due to travelling longer distances in the material), scattering (due to interactions with multiple particles, defects etc.), and sensor (each sensor adds its own filtering). Nevertheless, the simulation results provided do provide insights on the different failure mechanisms involved in this ductile fracture process.

5 | CONCLUSIONS

The investigation presented in this article focused on monitoring particle fracture in a particular precipitate hardened aluminium alloy, since it has been accepted and demonstrated that such type of small-scale fracture is a predominant source of damage during the early stages of the ductile fracture process. To the authors best knowledge, the progressive activation of such ductile fracture mechanism had not been investigated in situ and inside the volume. Consequently, the authors leveraged their prior related work and used the AE method in combination with both in situ SEM and in situ X-ray computer micro–computer tomography. The results presented confirm, for the first time that particle fracture indeed occurs throughout the volume and mostly before yielding, while void growth appears to dominate the ductile process post yielding. Aspects of the experimental findings were theoretically validated by a computational model capable of investigating the competing activation of particle versus matrix fracture at the scale of particle-matrix interface, while also providing associated wave propagation results.

ACKNOWLEDGEMENTS

A. Kontsos would like to acknowledge the financial support received by the Office of Naval Research under the Young Investigator Program, award #N00014-14-1-0571.

REFERENCES

1. Cuadra J, Baxevanakis KP, Mazzotti M, Bartoli I, Kontsos A. Energy dissipation via acoustic emission in ductile crack initiation. *Int J Fract*. 2016;199(1):89-104.

2. Grosskreuts J. Critical mechanisms in the development of fatigue cracks in 2024-T4 aluminum. in ICF2, Brighton (UK) 1969. 2013.
3. Kung C, Fine M. Fatigue crack initiation and microcrack growth in 2024-T4 and 2124-T4 aluminum alloys. *Metall Trans A*. 1979;10(5):603-610.
4. Roberts TM, Talebzadeh M. Acoustic emission monitoring of fatigue crack propagation. *J Constr Steel Res*. 2003;59(6):695-712.
5. Vanniamparambil P, Guclu U, Kontsos A. Identification of crack initiation in aluminum alloys using acoustic emission. *Exp Mech*. 2015;55(5):837-850.
6. Vanniamparambil PA, Bartoli I, Hazeli K, et al. An integrated structural health monitoring approach for crack growth monitoring. *J Intell Mater Syst Struct*. 2012;23(14):1563-1573.
7. Haynes RA, Habtour E, Henry TC, et al. Damage precursor indicator for aluminum 7075-T6 based on nonlinear dynamics. In: *Nonlinear Dynamics*. Vol.1 Cham: Springer; 2019:303-313.
8. Hazeli K, Askari H, Cuadra J, et al. Microstructure-sensitive investigation of magnesium alloy fatigue. *Int J Plast*. 2015;68:55-76.
9. Hazeli K, Cuadra J, Vanniamparambil PA, Kontsos A. In situ identification of twin-related bands near yielding in a magnesium alloy. *Scr Mater*. 2013;68(1):83-86.
10. Jin H, Lu WY, Haldar S, Bruck HA. Microscale characterization of granular deformation near a crack tip. *J Mater Sci*. 2011;46(20):6596-6602.
11. Hazeli K, Cuadra J, Streller F, et al. Three-dimensional effects of twinning in magnesium alloys. *Scr Mater*. 2015;100:9-12.
12. Cuadra J, Vanniamparambil PA, Servansky D, Bartoli I, Kontsos A. Acoustic emission source modeling using a data-driven approach. *J Sound Vib*. 2015;341:222-236.
13. Vanniamparambil PA, Cuadra J, Guclu U, Bartoli I, Kontsos A. Cross-validated detection of crack initiation in aerospace materials. in *SPIE Smart Structures and Materials+ Nondestructive Evaluation and Health Monitoring*. 2014. International Society for Optics and Photonics.
14. Baxevanakis KP, Wisner B, Schlenker S, Baid H, Kontsos A. Data-driven damage model based on nondestructive evaluation. *J Nondestruct Eval Diagn Progn Eng Syst*. 2018;1(3):031007.
15. Castaneda N, Wisner B, Cuadra J, Amini S, Kontsos A. Investigation of the Z-binder role in progressive damage of 3D woven composites. *Compos A: Appl Sci Manuf*. 2017;98:76-89.
16. Chmelık F, Pink E, Król J, Balık J, Pešička J, Lukáč P. Mechanisms of serrated flow in aluminium alloys with precipitates investigated by acoustic emission. *Acta Mater*. 1998;46(12):4435-4442.
17. Cousland SM, Scala C. Acoustic emission during the plastic deformation of aluminium alloys 2024 and 2124. *Mater Sci Eng A*. 1983;57(1):23-29.
18. Mazur K, Wisner B, Kontsos A. Fatigue damage assessment leveraging nondestructive evaluation data. *JOM*. 2018;70(7):1182-1189.
19. McBride S, MacLachlan J, Paradis B. Acoustic emission and inclusion fracture in 7075 aluminum alloys. *J Nondestruct Eval*. 1981;2(1):35-41.
20. Mo C, Wisner B, Cabal M, et al. Acoustic emission of deformation twinning in magnesium. *Materials*. 2016;9(8):662.
21. Mukherjee A, Hamstad M, Bianchetti R. Origin of burst-type acoustic emission in unflawed 7075-T6 aluminum. *J Test Eval*. 1976;4(5):313-318.
22. Wisner B, Kontsos A. Investigation of particle fracture during fatigue of aluminum 2024. *Int J Fatigue*. 2018;111:33-43.
23. Wisner B, Kontsos A. In situ monitoring of particle fracture in aluminium alloys. *Fatigue Fract Eng Mater Struct*. 2018;41(3):581-596.
24. Wisner B, Mazur K, Perumal V, et al. Acoustic emission signal processing framework to identify fracture in aluminum alloys. *Eng Fract Mech*. 2019;210:367-380.
25. Cuadra J, Vanniamparambil PA, Hazeli K, Bartoli I, Kontsos A. Damage quantification in polymer composites using a hybrid NDT approach. *Compos Sci Technol*. 2013;83:11-21.
26. Sause MGR. *In situ monitoring of fiber-reinforced composites: Theory, basic concepts, methods, and applications*. Vol. 242 Springer. Switzerland: Springer International Publishing AG; 2016.
27. Chung J-B, Kannatey-Asibu E. Acoustic emission from plastic deformation of a pure single crystal. *J Appl Phys*. 1992;72(5):1812-1820.
28. Frederick J, Felbeck D. Dislocation motion as a source of acoustic emission. In: *Acoustic Emission*. 100 Barr Harbor Drive, PO Box C700, West Conshohocken, PA, 19428-2959 USA: ASTM International; 1972.
29. Wisner B, Cabal M, Vanniamparambil PA, Hochhalter J, Leser WP, Kontsos A. In situ microscopic investigation to validate acoustic emission monitoring. *Exp Mech*. 2015;55(9):1705-1715.
30. Wisner B, Kontsos A. Fatigue damage precursor identification using nondestructive evaluation coupled with electron microscopy. In: *Fracture, Fatigue, Failure and Damage Evolution*. Vol.8 Cham: Springer; 2017:1-8.
31. Wisner BJ. Damage precursor identification via microstructure-sensitive nondestructive evaluation. 2017: Drexel University.
32. Morgeneyer TF, Taillandier-Thomas T, Helfen L, et al. In situ 3-D observation of early strain localization during failure of thin Al alloy (2198) sheet. *Acta Mater*. 2014;69:78-91.
33. Toda H. A 3D measurement procedure for internal local crack driving forces via synchrotron X-ray microtomography. *Acta Mater*. 2004;52(5):1305-1317.
34. Toda H, Yamamoto S, Kobayashi M, Uesugi K, Zhang H. Direct measurement procedure for three-dimensional local crack driving force using synchrotron X-ray microtomography. *Acta Mater*. 2008;56(20):6027-6039.
35. Zhang H, Toda H, Qu PC, et al. Three-dimensional fatigue crack growth behavior in an aluminum alloy investigated with in situ high-resolution synchrotron X-ray microtomography. *Acta Mater*. 2009;57(11):3287-3300.
36. Jespersen KM, Zangenberg J, Lowe T, Withers PJ, Mikkelsen LP. Fatigue damage assessment of uni-directional non-crimp

fabric reinforced polyester composite using X-ray computed tomography. *Compos Sci Technol*. 2016;136:94-103.

37. Toda H, Hidaka T, Kobayashi M, Uesugi K, Takeuchi A, Horikawa K. Growth behavior of hydrogen micropores in aluminum alloys during high-temperature exposure. *Acta Mater*. 2009;57(7):2277-2290.
38. Sause MGR. *On use of signal features for acoustic emission source identification in fibre-reinforced composites*. in *33rd European Conference on Acoustic EmissionTesting*. 2018. Senlis, France.
39. Kalafat S, Zelenyak AM, Sause MGR. *In-situ monitoring of composite failure by computing tomography and acoustic emission*, in *20th International Conference on Composite Materials*. 2015: Copenhagen.
40. Sause MGR. *Advances in in-situ monitoring of fiber reinforced composites*, in *17th European Conference of Composite Materials*. 2016: Munich, Germany.
41. Buchheit R, Grant RP, Hlava PF, Mckenzie B, Zender GL. Local dissolution phenomena associated with S phase (Al2CuMg) particles in aluminum alloy 2024-T3. *J Electrochem Soc*. 1997;144(8):2621-2628.
42. Huda Z, Taib NI, Zaharinie T. Characterization of 2024-T3: an aerospace aluminum alloy. *Mater Chem Phys*. 2009;113(2):515-517.
43. Zhang J, Huang YN, Mao C, Peng P. Structural, elastic and electronic properties of θ (Al 2 Cu) and S (Al 2 CuMg) strengthening precipitates in Al–Cu–Mg series alloys: first-principles calculations. *Solid State Commun*. 2012;152(23):2100-2104.
44. *Abaqus Analysis User's Guide*. Providence, RI, USA: Dassault Systèmes Simulia Corp; 2013.
45. Anand L, Kothari M. A computational procedure for rate-independent crystal plasticity. *J Mech Phys Solids*. 1996;44(4):525-558.
46. Nye JF. *Physical properties of crystals: their representation by tensors and matrices*. Oxford: Oxford university press; 1985.

APPENDIX A

The crystal behaviour of the aluminium matrix is captured using a rate-independent crystal plasticity user material subroutine developed by Anand and Kothari.[45] This is used to consider the different orientations of the aluminium crystal-with [001] being the "soft" orientation and [111] being the "hard" orientation. Using the constitutive relation from the subroutine, a boundary value problem is solved using the standard finite element method (Equation A1)

$$KU = F, \tag{A1}$$

where U and F are the displacement vector and the force vector respectively; K is the global stiffness matrix computed using the strain–displacement matrix $B^{(m)}$ and the constitutive relation matrix $C^{(m)}$ as shown in Equation A2

$$K = \sum_m \int_{V^{(m)}} B^{(m)T} C^{(m)} B^{(m)} dV^{(m)}. \tag{A2}$$

The analysis is run till the shear stress in the geometry attains the critically resolved shear stress for the aluminium matrix for the given orientation. This leads to the activation of the slip planes in the aluminium crystal, which lead to different strain localization for the considered orientations.[24] To identify where a fracture will occur and how the strain localization influences the location of fracture requires the model to be able to initiate fracture anywhere within the domain. An extended finite element formulation is used in which the domain is enriched using phantom nodes, thus allowing for independent fracture initiation anywhere within the domain if it meets the required mesh resolution.[44] To incorporate the enriched formulation, the output of the crystal plasticity model is transferred to a continuum plasticity model. The continuum homogeneous material property of the aluminium matrix for the given single crystal orientation is computed using Equation A3.[46]

$$\begin{aligned}\frac{1}{E_{\{uvw\}}} &= s_{11}^{'} \\ &= s_{11} - 2\left(s_{11} - s_{12} - \frac{1}{2}s_{44}\right)\left(l_1^2 l_2^2 + l_2^2 l_3^2 + l_1^2 l_3^2\right),\end{aligned} \tag{A3}$$

where $E_{\{uvw\}}$ is the elastic modulus in the $\{uvw\}$ direction; s_{11}, s_{12}, and s_{44} are the components of the compliance tensor S; and l_1, l_2, and l_3 are the direction cosines of the loading axis with respect to the crystal coordinate axes. The deformed mesh from the previous model is used as the geometry input for the new analysis. The stress state from the crystal plasticity is applied as the initial stress state, τ^I, of the new analysis. The new stress state, τ, is therefore computed as shown in Equation A4.

$$\tau^{(m)} = C^{(m)}\varepsilon^{(m)} + \tau^{I(m)}, \tag{A4}$$

where ε is the strain computed in the new analysis. A number of equilibrating increments is required to check and allow for equilibrium of the new model after the introduction of the stress state of the crystal plasticity model as an initial stress state. A damage initiation

criterion was assigned to initiate fracture. Thereafter, the loading is continued till the fracture occurs.

As seen in the paper by Wisner et al,[24] the location of the fracture varies depending on the crystal orientation of the aluminium matrix. These models were run in 50 μm matrix domain with a particle embedded in the centre of size 10 μm. A uniaxial loading with a displacement of 1 μm for the CP model and 0.33 μm for the continuum model were applied on the nodes and the opposite face was constrained. The whole domain was discretized to 10 688 elements.

To study the effect of wave propagation without the effect of reflections, a 1 mm (=1000 μm) cubic domain was considered. To reduce computational cost, an octant domain was studied. To incorporate the enriched formulation, the domain near the particle was considered as an implicit domain and the remaining volume was set as an explicit one. The domains were concurrently coupled for the structural analysis. The domain was loaded to a displacement of 1.729 μm to attain the stress state required for fracture. Thereafter, this model was transferred to the co-simulation domain and a quasi-static uniaxial loading of 0.068 nm was considered for a duration of 0.05 ns. The model was loaded till the fracture event occurred. As soon as the crack increment was completed, it was switched to a new dynamic step where the load was held constant and the energy released from the fracture was allowed to propagate as stress waves for a duration of 0.1 μs.